Table 1 Structural properties

Alloy	σ (tensile yield) $\times 10^3$ psi[a]					E (tensile) $\times 10^6$ psi[a]				
	Room temp.	400°F	600°F	800°F	1000°F	Room temp.	400°F	600°F	800°F	1000°F
Al-2024-T86	67.0	50.3	...	...	...	10.5	9.5	...	...	...
Ti-8Al-1Mo-1V	125.0	93.8	87.5	75.0	65.0	18.5	16.8	16.3	14.6	12.2
Ti-6Al-4V	150.0	103.5	96.0	88.5	72.0	16.0	14.2	13.1	11.9	8.0
Ti-5Al-4FeCr	150.0	115.5	103.5	91.5	72.0	16.5	14.5	13.7	12.5	Not available

[a] Strengths are for temperature exposure from ½ to 1 hr.

aluminum alloys. Many useful criteria have been established with which to evaluate these alloys from the standpoint of structural strength and fatigue life. Flutter characteristics represent yet another area to be considered. A flutter ratio is developed below for the purpose of comparing the flutter properties of titanium alloys to those of aluminum alloys.

Flutter Ratio

Given a specific flight vehicle configuration designed in aluminum, it is desired to compare its flutter characteristics to those of the same vehicle designed in titanium. Hence, for the purpose of this development, the external load distribution, the vehicle planform, and the parameter c are assumed to be constant for both configurations. Using these assumptions, the flexural strength equation

$$\sigma = Mc/I \tag{1}$$

yields

$$\sigma_A/\sigma_T = I_T/I_A \tag{2}$$

where the subscripts A and T refer to aluminum and titanium, respectively. The general equation for the fundamental frequency of a beam is

$$\omega = K(EI/w)^{1/2} \tag{3}$$

Placing Eq. (2) into a similar ratio formed from Eq. (3) yields

$$\omega_A^2/\omega_T^2 = E_A\sigma_T w_T/E_T\sigma_A w_A \tag{4}$$

Although Eq. (4) expresses the ratio of bending frequencies, it should be noted that the torsional frequencies would be in approximately the same ratio. Let

$$\psi = \frac{V_T/b_T\omega_T\mu_T^{1/2}}{V_A/b_A\omega_A\mu_A^{1/2}} \tag{5}$$

where $V/b\omega\mu^{1/2}$ is the well-known dimensionless flutter parameter. Placing Eq. (4) into Eq. (5) yields the flutter parameter ratio

$$\psi = (E_A\sigma_T/E_T\sigma_A)^{1/2} \tag{6}$$

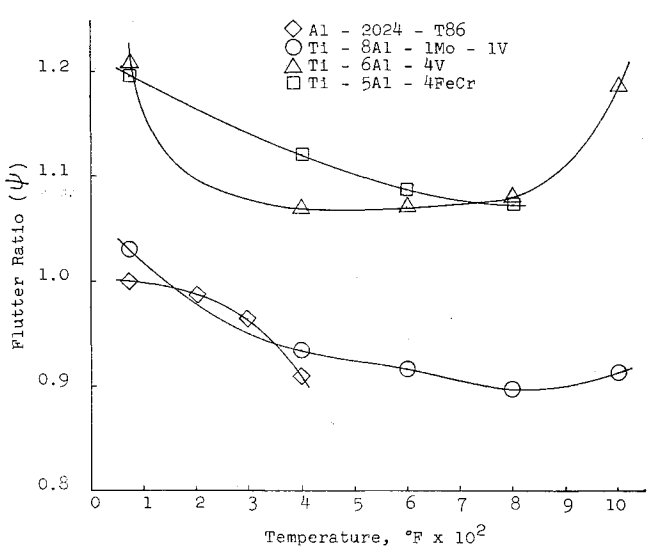

Fig. 1 Flutter ratio vs temperature for constant reference value of E_A/σ_A at room temperature.

Example

Table 1 lists the structural properties of a standard aluminum alloy and those of a number of titanium alloys currently being considered for use in aircraft structures. Figure 1 contains curves of ψ vs temperature for each of the alloys considered. ψ was computed keeping the ratio E_A/σ_A as a constant reference value, at room temperature.

Concluding Remarks

It should be noted that the development presented herein was based on a predetermined set of conditions. However, as can be seen, the method itself is general. It is recognized that other considerations would dictate changes in the structural design when converting from one material to another. Thus, Fig. 1 illustrates the change in flutter characteristics that result from substituting titanium for aluminum while designing for the same percent of yield stress.

Equations of Motion for Spin Stabilization Analysis in Terms of Euler Angles

PHILIP S. CARROLL*
The Bendix Corporation, Ann Arbor, Mich.

MOST of the literature on spin stabilization analysis of space vehicles approaches the problem by first solving the Euler equations of rotational motion in terms of body rates (see Ref. 1 for a recent example). This approach has been especially prevalent when the spinning body is influenced by external torques, which are usually expressed in body coordinates. When necessary, the analyses then proceed with coordinate transformations of the body rates into Euler-angle rates so that subsequent integration will result in analytical time histories of the spin-axis Euler angles with respect to inertial space. A classic example of this latter step is presented in Ref. 2.

The purpose of this note is to improve upon the preceding procedure of spin stabilization analysis by deriving linearized equations of satellite rotational motion directly in terms of Euler angles. The equations will include terms containing external torques so that substitution of proper expressions for these torques will allow direct solution for a variety of cases, such as responses to impulsive control torques or natural disturbance torques.

Received April 9, 1964

* Supervisor, Control and Stabilization Section, Bendix Systems Division. Member AIAA.

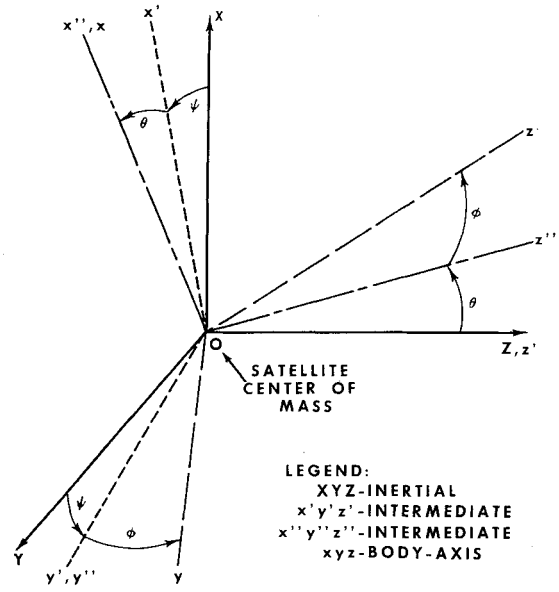

Fig. 1 Euler-angle rotations from inertial coordinate system to body-axis coordinate system.

Angular motion of a symmetric satellite is well described by the classical Euler equations of motion of a rigid body about principal axes in an orthogonal body-axis coordinate system. Thus,

$$I_x\dot{\omega}_x + (I_z - I_y)\omega_y\omega_z = T_x \tag{1}$$

$$I_y\dot{\omega}_y + (I_x - I_z)\omega_z\omega_x = T_y \tag{2}$$

$$I_z\dot{\omega}_z + (I_y - I_x)\omega_y\omega_x = T_z \tag{3}$$

where

I_x, I_y, I_z = principal moments of inertia, slug-ft^2
$\omega_x, \omega_y, \omega_z$ = angular rates about the body axes, rad/sec
T_x, T_y, T_z = external torques about the body axes, ft-lb

The x axis is designated as the spin axis and the torque about it is assumed to be zero ($T_x = 0$). Usually, this is essentially true except for the torques causing spin rate decay, which can be neglected in most cases if the time period of interest is short. Also, the transverse-axis moments of inertia are assumed equal ($I_y = I_z = I_t$), which is typically the case. Thus, Eq. (1) is reduced to a single term

$$I_x\dot{\omega}_x = 0 \tag{4}$$

and it is seen that spin rate is a constant ($\omega_x = \omega_s$). If the spin axis moment of inertia is designated by I_s, the moment-of-inertia ratio is given by

$$\sigma = I_s/I_t \tag{5}$$

Then the linearized Euler equations become

$$\dot{\omega}_y + (\sigma - 1)\omega_s\omega_z = T_y/I_t \tag{6}$$

$$\dot{\omega}_z - (\sigma - 1)\omega_s\omega_y = T_z/I_t \tag{7}$$

In order to express the motion relative to an inertial coordinate system, it is necessary to define Euler angles between the inertial and body-axis coordinate systems. Any inertial coordinate system centered at the satellite center of mass may be chosen, although there is usually one that simplifies the disturbance torque derivations and that is most convenient for graphical expression of final results. Ordinarily, the x axis of the inertial frame will be coincident with the initial orientation of the spin axis. When the spin axis has drifted slightly from its initial orientation, the relative orientations of the inertial and body-axis coordinate systems will be as shown in Fig. 1. Conventional Euler angle rotations are employed: ψ about Z to an intermediate $x'y'z'$ set, θ about y' to an intermediate $x''y''z''$ set, and ϕ about x'' to the final xyz body-axis set.

By projection of the components of satellite angular velocity ($\omega_x, \omega_y, \omega_z$) onto the y' and z'' axes, and equating to the instantaneous components of Euler-angle rates $\dot{\theta}$ and $\cos\theta\dot{\psi}$, respectively, the Euler-angle rate equations are derived as follows:

$$\dot{\theta} = \omega_y\cos\phi - \omega_z\sin\phi \tag{8}$$

$$\cos\theta\dot{\psi} = \omega_z\cos\phi + \omega_y\sin\phi \tag{9}$$

Further, by instantaneous projection of the Euler-angle rates onto the x axis, it is seen that

$$\omega_s = \dot{\phi} - \dot{\psi}\sin\theta \tag{10}$$

At this point, the small-angle approximation may be applied, and all second-order terms may be neglected. The assumption of small angles is valid out to about 15°, and even well beyond that the results give good qualitative indication of spin-axis motion.

Now, integration of Eq. (10) gives

$$\phi = \omega_s t \tag{11}$$

and the final, linearized Euler-angle rate equations become

$$\dot{\theta} = \omega_y\cos\omega_s t - \omega_z\sin\omega_s t \tag{12}$$

$$\dot{\psi} = \omega_z\cos\omega_s t + \omega_y\sin\omega_s t \tag{13}$$

Finally, differentiate Eqs. (12) and (13) and substitute Eqs. (6) and (7) into them. After simplifying, the linearized equations of motion in terms of Euler angles are finally obtained as follows:

$$\ddot{\theta} = -\sigma\omega_s\dot{\psi} + (T_y/I_t)\cos\omega_s t - (T_z/I_t)\sin\omega_s t \tag{14}$$

$$\ddot{\psi} = \sigma\omega_s\dot{\theta} + (T_z/I_t)\cos\omega_s t + (T_y/I_t)\sin\omega_s t \tag{15}$$

As mentioned previously, these equations are valid for angle θ and ψ as large as 15°, and they give reasonable qualitative solutions for much larger angles.

When the body-fixed torques T_y and T_z about the transverse axes are zero, the remaining terms of Eqs. (14) and (15) provide accurate solutions for the typical high-frequency, low-amplitude nutations that occur in response to initial angular rates. When the external torques do apply, their effects are essentially superimposed on the nutations (also known as free precession, coning, or wobble). The superposition is not always linear because the torques are often expressed in terms of the dependent variables θ and ψ which change the form of the homogeneous equation. This usually occurs for the various disturbance torques that vary as a function of spin-axis orientation. In spite of the equation changes, superposition can almost always be used, and, therefore, the initial angular rates need not be included in the solutions with external torques.

It is interesting to note that the sinusoidal torque terms appear to be equivalent to inertially fixed torques that vary in magnitude only. In many cases, the gravity-gradient and magnetic torques represented by T_y and T_z are sinusoidal themselves at the spin frequency, so that the torque terms often cancel or simplify to linear functions of the Euler angles. In fact, this situation is usually the case for circular orbits, and thus Eqs. (14) and (15) can often be solved quite readily as linear, time-invariant differential equations.

The solutions are most readily visualized by plots in the $\theta - \psi$ plane. These plots are equivalent to the trace of the spin axis on a plane normal to the initial orientation of the spin axis. Responses due to impulsive control torques usually appear as small connected circles in the $\theta - \psi$ plane, whereas responses due to disturbance torques are ellipses or exponential curves. It can be shown by comparisons with simulation results that such plots are very accurately representative of

actual responses, even when the spin axis drift has violated the small-angle approximation appreciably.

References

[1] Wheeler, P. C., "Two-pulse attitude control of an asymmetric spinning satellite," AIAA Preprint 63-338 (August 1963).

[2] Suddath, J. H., "A theoretical study of the angular motions of spinning bodies in space," NASA TR R-83 (1960).

Growth of the Turbulent Inner Wake behind 3-In.-Diam Spheres

R. Knystautas*

Canadian Armament Research and Development Establishment, Valcartier, Quebec, Canada

THERE have been a number of experiments carried out at several laboratories to measure the growth of the turbulent inner wake behind hypervelocity spheres. The available literature indicates that the spheres investigated have not exceeded $\frac{1}{2}$ in. in diameter. For example, Slattery and Clay[1] have studied wakes behind $\frac{1}{4}$- and $\frac{1}{2}$-in.-diam solid aluminum spheres that have been launched at a velocity of 9000 fps into air at pressures ranging from 40 to 760 mm Hg. For the atmosphere data, a $\frac{1}{2}$-power dependence of wake width upon length is apparent. The lower pressure data exhibit $\frac{1}{2}$-power dependence for the first 50 body diameters, and then a $\frac{1}{3}$-power dependence seems to be better. Dana and Short[2] studied the turbulent wake behind 0.22- and 0.31-in.-diam aluminum spheres launched at velocities from 2000 to 9000 fps into atmospheric air. The measured growth rate is in good agreement with the theory of Lees and Hromas.[3] More recently, Murphy and Dickinson[4] have launched $\frac{1}{8}$- and $\frac{1}{4}$-in.-diam spheres at muzzle velocities of 7100 and 6400 fps, respectively, into atmospheric air. From the results, they concluded that 1) the data, by least-squares fit, are well represented by a $\frac{1}{2}$-power dependence of width on length for the entire length of wake; 2) the data can also be represented by a $\frac{1}{3}$-power dependence, which shows a change in the growth rate at about 150–200 body diameters, the initial growth rate being less than the one further downstream; and 3) there may be a scaling effect in the growth rate with projectile size.

In the present experiments, the width of the turbulent inner wake behind 3-in.-diam solid aluminum spheres was measured for wake lengths extending up to 1500 body diameters. The spheres were launched into atmospheric air from a conventional solid propellant gun at a muzzle velocity of 6700 fps. The wake was photographed at three schlieren and ten shadowgraph stations of the CARDE Aeroballistics Range which were triggered simultaneously when the sphere passed a predetermined downrange station.

The data were reduced by measuring the width of the wake from the schlieren and shadowgraph photographs at longitudinal intervals of $\frac{1}{4}$ or $\frac{1}{2}$ body diameter. To even out irregularities in the measured width due to turbulence, the measurements thus obtained were averaged for stretches of wake of approximately 5 body diameters in length and were nondimensionalized with respect to the body diameter for presentation. In order to locate correctly a particular transverse wake dimension relative to the projectile, a correction to the longitudinal wake dimension was applied, as in the experiments of Murphy and Dickinson. The correction accounts for the apparent shortening of the longitudinal dimension due to projectile deceleration. It must also be noted here that, in the analysis of the data, the interaction of the reflected bow shock wave with the turbulent wake, and in particular the effect of this on the growth rate, has not been taken into account. In these experiments, however, the initial 180 body diameters of wake are free of disturbances caused by the reflected bow shock wave.

Received April 13, 1964. This work was administered by the Aerophysics Wing, Canadian Armament Research and Development Establishment and was supported partly by the Advanced Research Projects Agency under Order 133. The author is indebted to H. M. McMahon, Head, Aerodynamics Section, Aerophysics Wing, for his numerous suggestions and constructive criticism.

* Scientific Officer. Member AIAA.

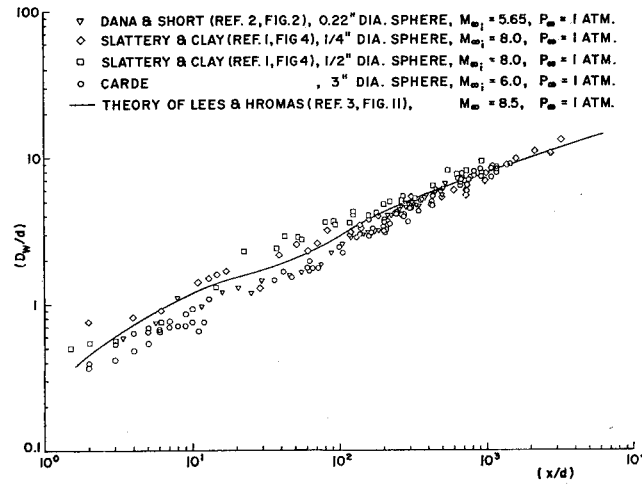

Fig. 1 The growth of the turbulent inner wake behind spheres (wake width vs wake length).

Experimental evidence indicates that the growth of the hypersonic turbulent wake can be described by a relationship of the form $(D_w/d) \propto (x/d)^n$. Theoretical analyses indicate that $n = \frac{1}{3}$ is asymptotically approached in the far wake. Figure 1 shows a logarithmic plot of the turbulent wake width D_w/d measured behind various sizes of spheres against the wake length x/d. For $x/d < 200$, there is some variation when a set of data from one source is compared with that from another. In the region $x/d < 200$, the 3-in.-diam data seem to follow closely the data of Dana and Short. The data of Slattery and Clay generally fall above in this region. For $x/d > 200$, all of the data agree quite well with each other, and the tendency is to approach a $\frac{1}{3}$-power dependence of width on length. (Unfortunately, the data of Murphy and Dickinson were not available in a form that could be replotted for comparison.)

The same 3-in.-diam sphere data are plotted in Fig. 2, the abscissa in this case being $(x/d)^{1/3}$. In this figure, one of the two presently available theoretical curves calculated by Lees and Hromas for a sphere with $M_\infty = 8.5$, $p_\infty = 1$ atm is also

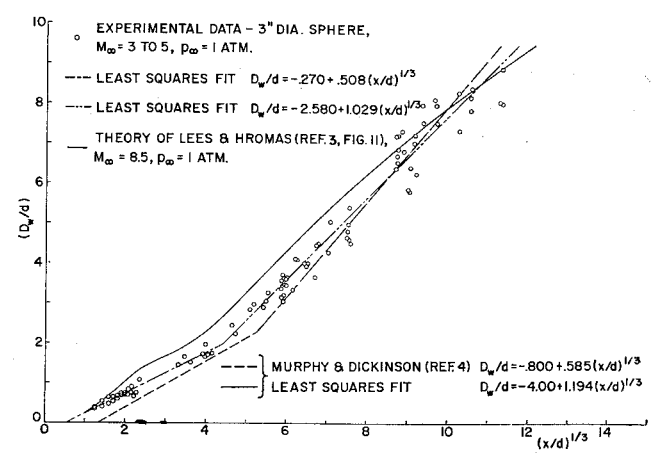

Fig. 2 The growth of the turbulent inner wake behind spheres (wake width vs wake length$^{1/3}$).